Methane carbon dioxide reforming for hydrogen production in a compact reformer – a modeling study

Meng Ni [*]

Building Energy Research Group, Department of Building and Real Estate,
The Hong Kong Polytechnic University, Hung Hom, Kowloon, Hong Kong, P.R. China

Abstract. Methane carbon dioxide reforming (MCDR) is a promising way of utilizing greenhouse gas for hydrogen-rich fuel production. Compared with other types of reactors, Compact Reformers (CRs) are efficient for fuel processing. In a CR, a thin solid plate is placed between two porous catalyst layers to enable efficient heat transfer between the two catalyst layers. In this study, the physical and chemical processes of MCDR in a CR are studied numerically with a 2D numerical model. The model considers the multi-component gas transport and heat transfer in the fuel channel and the porous catalyst layer, and the MCDR reaction kinetics in the catalyst layer. The finite volume method (FVM) is used for discretizing the governing equations. The SIMPLEC algorithm is used to couple the pressure and the velocity. Parametrical simulations are conducted to analyze in detail the effects of various operating/structural parameters on the fuel processing behavior.

Keywords: compact reformer; fuel processing; porous media; hydrogen production; methane carbon dioxide reforming

1. Introduction

Hydrogen is an ideal energy carrier (Ni *et al*. 2006). It can be converted into electricity efficiently by a fuel cell with water as the by-product (Mermelstain *et al*. 2009, Rady *et al*. 2012). In addition to hydrogen storage, another challenge for hydrogen energy and fuel cell is to produce hydrogen efficiently at a large scale. In the long run, hydrogen should be produced from renewable resources, such as from water by solar photocatalytic water splitting, solar thermochemical water-splitting, or from solar cell driven water electrolysis (Ni *et al*. 2007, 2008, Sheffe and Steinfeld 2012). However, the efficiencies of photocatalysis and thermochemical cycles are still too low to be economically competitive. The high cost of solar cells and electrolyzers also impedes large scale applications. For comparison, hydrogen production from hydrocarbon fuels (i.e., methane) is efficient and can be a feasible way for large-scale hydrogen production for the near future (Chanburanasiri *et al*. 2013, Yuan *et al*. 2010, Zeppieri *et al*. 2010). Conventionally, hydrogen can be produced from methane by one of these processes: (1) methane steam reforming (MSR); (2) partial oxidation (POX); and (3) autothermal reforming (ATR) (Ahmed and Foger

---

∗Corresponding author, Associate Professor , E-mail: bsmengni@polyu.edu.hk

2010, Halabi *et al*. 2008, Yuan *et al*. 2007a). MSR is a common method for fuel processing at a large scale. In MSR reaction (Eq. (1)), steam molecules react with methane molecules on the catalyst surface to produce hydrogen and carbon monoxide. The carbon monoxide produced can further react with steam to produce additional hydrogen (Eq. (2)), which is called water gas shift reaction (WGSR).

$$CH_4 + H_2O \leftrightarrow CO + 3H_2 \tag{1}$$

$$CO + H_2O \leftrightarrow CO_2 + H_2 \tag{2}$$

In addition to MSR, POX, and ATR, methane carbon dioxide reforming (MCDR) has been proposed and demonstrated to be feasible for hydrogen-rich gas production (Eq. (3)) (Huang *et al*. 2011, Lemonidou *et al*. 1998, Li *et al*. 2011, Richardson and Paripatyadar 1990, Yu *et al*. 2012).

The idea is very interesting as it offers an alternative way of utilizing green-house gas (CO_2) for fuel processing.

$$CO_2 + CH_4 \leftrightarrow 2CO + 2H_2 \tag{3}$$

The H_2 molecules produced from MCDR can react with CO_2 to form CO and H_2O (reversed WGSR, Eq. (2)). Further, the existence of H_2O may initiate MSR reaction (Eq. (1)).
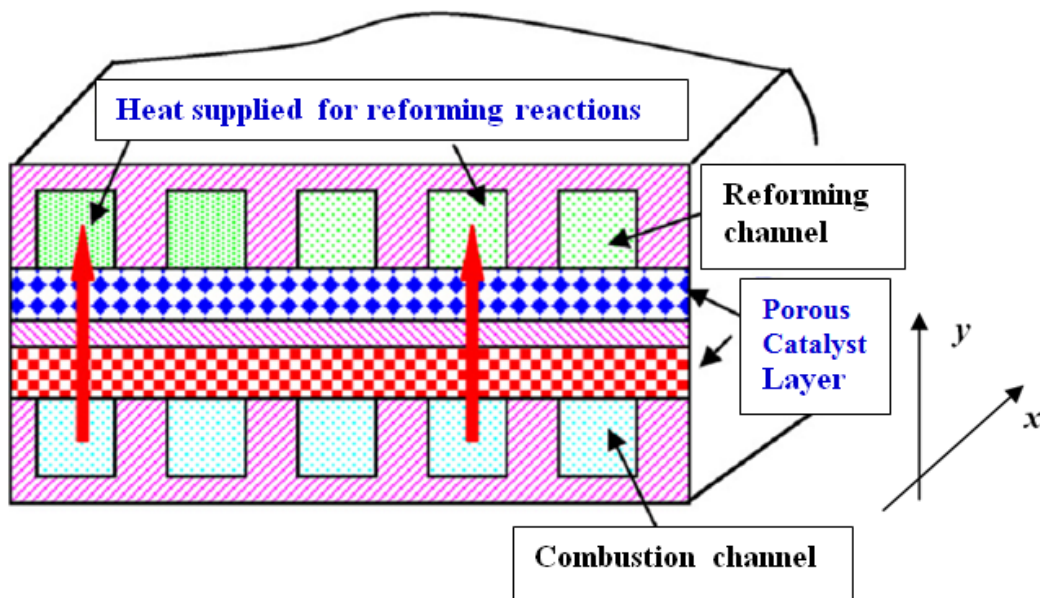

Fig. 1 A typical compact reformer (CR) (adapted from Yuan *et al*. 2007a)

The reforming reactions and shift reaction can be accomplished in various types of chemical reactors (Abashar *et al.* 2003, Gallucci *et al.* 2013, Lulianelli *et al.* 2010). Among many reactors, compact reformer (CR) is very promising for various fuel processing or energy conversion processes. A CR consists of two catalyst layers separated by a thin solid plate, as shown in Fig. 1 (adapted from Yuan *et al.* 2007a). The use of thin plate allows efficient heat transfer from the combustion channel to the fuel reforming channel and separates the two gas streams. The CRs can achieve high volumetric power density due to their compactness nature. As a result, CRs are suitable for stationary and transportation applications (Yuan *et al.* 2007b, Zanfir and Gavrillidis 2003). Although some preliminary studies have been performed for CRs for fuel processing, no study has been performed on CRs for hydrogen production by methane carbon dioxide reforming. It's also unclear to what extent the reversed WGSR and MSR reactions affect the MCDR reaction, and how the change in inlet temperature and catalyst thickness can influence the coupled transport and reaction kinetics in the reformer. A fundamental understanding of the complicated physical chemical processes is important for optimization of the reformer operating and structural parameters for efficient fuel processing.

Compared with experimental study, mathematical modeling is an economical and powerful tool to understand the fundamental processes in the reactor. After a mathematical model is validated, the performance of the reactor can be predicted easily by simply adjusting the simulation parameters (Hosseini *et al.* 2011, Lebouvier *et al.* 2011, Lim *et al.* 2005, Wang *et al.* 2010).

Moreover, mathematical models can provide very detailed information that may be very difficult to obtain from experimental investigations. For example, it's almost impossible (based on existing technology) to explore the detailed gas species' distribution and temperature distribution in the porous catalyst experimentally. For comparison, the information can be easily obtained with a mathematical model (Al-Baghdadi and Al-Janabi 2007, Ni 2011, 2012a, Qi *et al.* 2008).

In this paper, the performance of a CR for hydrogen-rich gas production from CO_2/CH_4 gas mixture is studied numerically with a 2D mathematical model. The model considers the heat and mass transfer in the fuel reforming channel and the catalyst layer, as well as the chemical reaction kinetics in the porous catalyst layer. The simulation results are compared with experimental data from the literature for model validation. Parametrical simulations are performed to understand the coupled transport and reaction phenomena in the CR and to investigate how the operating/structural parameters affect the CR performance.

2. Model development

A 2D mathematical model is developed to simulate the CR used for hydrogen-rich gas production from CO_2/CH_4 mixture. As the focus of the present paper is to examine the processes in the fuel reforming side, heat from the combustion channel is supplied to the catalyst layer for fuel processing via the thin solid plate and it is specified as a boundary condition (Yuan *et al.* 2007a). Here we consider a fuel reforming channel from a CR stack. Neglecting the 3D effect, the operating principle can be shown in Fig. 2. The computational domain includes the thin solid plate, the catalyst layer for fuel processing and the reforming channel. To describe the complicated transport and reaction phenomena in the CR, the 2D model consists of a computational fluid dynamics (CFD) model and a chemical model. The chemical sub-model is developed to determine the reaction rates and corresponding reaction heats. The CFD sub-model is used to simulate the fluid flow and heat/mass transfer in the fuel channel and the porous catalyst layer.
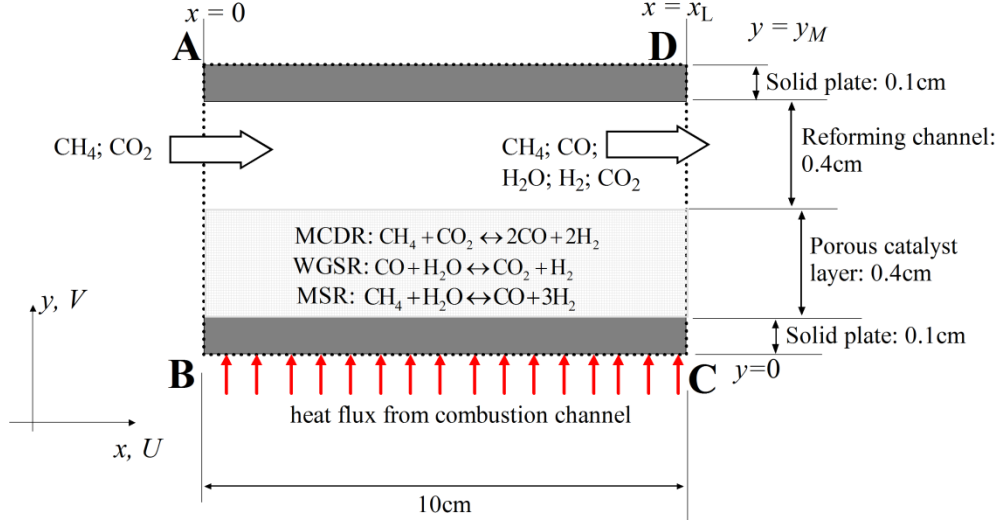
Fig. 2 Schematic of the computational domain

2.1 Chemical model

In operation, CH_4/CO_2 gas mixture is supplied to the fuel reforming channel. The gas species are then transported from the fuel channel into the porous catalyst layer. It is assumed that chemical reactions only occur in the catalyst layer while the reaction in the fuel channel is negligibly small. In the present study, MCDR, WGSR, and MSR are all considered. The CH_4 pyrolysis ($CH_4 \leftrightarrow C + 2H_2$) and Boudouard reaction ($2CO \leftrightarrow C + CO_2$) are not considered due to their relatively low reaction rate compared with the other 3 reactions. However, it should be mentioned that in practical operation, the CH_4 pyrolysis and Boudouard reactions can occur on the catalyst surface under certain conditions, which can cause carbon deposition and catalyst degradation (Goula *et al*. 2006, Papadam *et al*. 2012). Thus, these detrimental reactions will be included in a subsequent study.

A few research groups have measured the reaction rates of MCDR (Gokon *et al*. 2009, Moon and Ryu 2003, Richardson and Paripatyadar 1990, Soloviev *et al*. 2011). It's found that the Langmuir-Hinshelwood (LH) model can provide a better fitting with the experimental results, thus it's used in the present study. According to the LH model, the reaction rate of MCDR (R_{MCDR}, mol.m^{-3}.s^{-1}) can be written as (Gokon *et al*. 2009)

$$R_{MCDR} = \frac{k_{co_2} K_{CO_2} K_{CH_4} P_{CO_2} P_{CH_4}}{(1 + K_{CO_2} P_{CO_2} + K_{CH_4} P_{CH_4})^2} \tag{4}$$

$$k_{CO_2} = 1.17 \times 10^7 \exp\left(-\frac{83,498}{RT}\right), \quad \left(mol \cdot m^{-3} \cdot s^{-1}\right) \tag{5}$$

$$K_{CO_2} = 3.11 \times 10^{-3} \exp\left(\frac{49,220}{RT}\right), \quad atm^{-1} \tag{6}$$

$$K_{CH_4} = 0.653 \exp\left(\frac{16,054}{RT}\right), \quad atm^{-1} \tag{7}$$

where P_{CO_2} and P_{CH_4} are the partial pressure of CO_2 and CH_4 in atm. T is the temperature (K). R is the universal gas constant (8.3145 J.mol^{-1}K^{-1}).

The formulas proposed by Haberman and Young (Haberman and Young 2004) have been frequently used for calculating the MSR and WGSR reaction rates due to their good agreement with the experiments. According to their model, the reaction rates (mol.m^{-3}.s^{-1}) of MSR (R_{MSR}) and WGSR (R_{WGSR}) can be determined as

$$R_{MSR} = k_{rf}\left(P_{CH_4}P_{H_2O} - \frac{P_{CO}\left(P_{H_2}\right)^3}{K_{ps}}\right) \tag{8}$$

$$k_{rf} = 2395 \exp\left(\frac{-231266}{RT}\right) \tag{9}$$

$$K_{pr} = 1.0267 \times 10^{10} \times \exp\left(-0.2513Z^4 + 0.3665Z^3 + 0.5810Z^2 - 27.134Z + 3.277\right) \tag{10}$$

$$R_{WGSR} = k_{sf}\left(P_{CO}P_{H_2O} - \frac{P_{CO_2}P_{H_2}}{K_{ps}}\right) \tag{11}$$

$$k_{sf} = 0.0171 \exp\left(\frac{-103191}{RT}\right) \tag{12}$$

$$K_{ps} = \exp\left(-0.2935Z^3 + 0.6351Z^2 + 4.1788Z + 0.3169\right) \tag{13}$$

$$Z = \frac{1000}{T(K)} - 1 \tag{14}$$

where P is partial pressures of gas species in Pa.

As the reaction heat for the endothermic MCDR reaction is about 256.8 kJ.mol^{-1} at 600 K and 260.05 kJ.mol^{-1} at 1200 K (Chase 1998), the reaction heat (consumption) of MCDR (H_{MCDR}, J.mol^{-1}) determined as (assuming linear dependence on temperature)

$$H_{MCDR} = -(253550.0 + 5.41667T)$$
(15)

Similarly, the reaction heats for exothermic WGSR and endothermic MSR can be determined using corresponding enthalpy changes (Chase 1998). Assuming linear dependence on temperature in the range of 600 K – 1200 K, the reaction heats for MSR reaction (H_{MSR}, J.mol^{-1}) and WGSR (H_{WGSR}, J.mol^{-1}) can be calculated as (Ni 2012b).

$$H_{MSR} = -(206205.5 + 19.5175T)$$
(16)

$$H_{WGSR} = 45063 - 10.28T$$
(17)

2.2. Computational Fluid Dynamics (CFD) model

The CFD sub-model is used to simulate the heat and mass transfer in the fuel channel and the catalyst layer. Due to the low velocity and small size of the reformer, the flow in the channel is typically laminar. Local thermal equilibrium is also assumed, that is, the temperature of gas and the solid catalyst are locally the same. As a result, only one energy equation is needed. Heat radiation effect is assumed to be small. All reactants/products are assumed to be ideal gases. Based on the above assumptions, the governing equations for the CFD model include the conservation laws of mass, momentum, energy and species (Wang 2004).

$$\frac{\partial(\rho U)}{\partial x} + \frac{\partial(\rho V)}{\partial y} = 0$$
(18)

$$\frac{\partial(\rho UU)}{\partial x} + \frac{\partial(\rho VU)}{\partial y} = -\frac{\partial P}{\partial x} + \frac{\partial}{\partial x}\left(\mu\frac{\partial U}{\partial x}\right) + \frac{\partial}{\partial y}\left(\mu\frac{\partial U}{\partial y}\right) + S_x$$
(19)

$$\frac{\partial(\rho UV)}{\partial x} + \frac{\partial(\rho VV)}{\partial y} = -\frac{\partial P}{\partial y} + \frac{\partial}{\partial x}\left(\mu\frac{\partial V}{\partial x}\right) + \frac{\partial}{\partial y}\left(\mu\frac{\partial V}{\partial y}\right) + S_y$$
(20)

$$\frac{\partial(\rho c_P UT)}{\partial x} + \frac{\partial(\rho c_P VT)}{\partial y} = \frac{\partial}{\partial x}\left(k\frac{\partial T}{\partial x}\right) + \frac{\partial}{\partial y}\left(k\frac{\partial T}{\partial y}\right) + S_T$$
(21)

$$\frac{\partial(\rho UY_i)}{\partial x} + \frac{\partial(\rho VY_i)}{\partial y} = \frac{\partial}{\partial x}\left(\rho D_{i,m}^{eff}\frac{\partial Y_i}{\partial x}\right) + \frac{\partial}{\partial y}\left(\rho D_{i,m}^{eff}\frac{\partial Y_i}{\partial y}\right) + S_{sp}$$
(22)

where U and V are the velocity components in x and y directions respectively.

The density of the gas mixture (ρ) depends on the mass fraction of each component (Y_i) and can be written as (Ni 2012a, Reid *et al*. 1987).

$$\rho = \frac{1}{\sum_{i=1}^{N} Y_i / \rho_i} \tag{23}$$

where ρ_i is the density of gas species i and can be determined from the ideal gas law.

$$\rho_i = \rho_{i,298K} \frac{298}{T} \tag{24}$$

The mass fraction of species i (Y_i) can be determined from its molar fraction (X_i) as

$$Y_i = X_i \left(\frac{M_i}{\sum_{i=1}^{N} X_i M_i} \right) \tag{25}$$

where M_i is molecular weight of species i (kg.kmol^{-1}).

The viscosity of the gas mixture (μ) can be determined using the mass fraction and viscosity (μ_i) of each fluid component (Reid *et al*. 1987)

$$\mu = \sum_{i=1}^{n} \frac{Y_i \mu_i}{\sum_{j=1}^{n} \left(Y_j \sqrt{\frac{M_j}{M_i}} \right)} \tag{26}$$

k_{eff} and $c_{p,eff}$ are the effective heat conductivity (W.m^{-1}.K^{-1}) and effective heat capacity (J.kg^{-1}.K^{-1}). In the porous catalyst layer, k_{eff} and $c_{p,eff}$ depend on the porosity of the catalyst layer (ε) (Ni 2012b, Yuan *et al*. 2003)

$$k_{eff} = \varepsilon k_f + (1-\varepsilon) k_s \tag{27}$$

$$c_{p,eff} = \varepsilon c_{p,f} + (1-\varepsilon) c_{p,s} \tag{28}$$

where k_f and k_s are the heat conductivities of the gas and the solid catalyst, respectively. $c_{p,f}$ and $c_{p,s}$ represent the heat capacities of the gas and the solid catalyst, respectively.

The effective diffusion coefficient of species i ($D_{i,m}^{eff}$) can be determined as (Ni 2012b, Reid *et al.* 1987)

$$\frac{1}{D_{i,m}^{eff}} = \begin{cases} \dfrac{\xi}{\varepsilon}\left(\dfrac{\displaystyle\sum_{j\neq i}\dfrac{X_j}{D_{ij}}}{1-X_i} + \dfrac{3}{2r_p}\sqrt{\dfrac{\pi M_i}{8RT}} \right), & \text{in the porous catalyst layer} \\[4ex] \dfrac{\displaystyle\sum_{j\neq i}\dfrac{X_j}{D_{ij}}}{1-X_i}, & \text{in the fuel channel} \end{cases} \tag{29}$$

$$D_{ij} = \frac{0.0026T^{1.5}}{p\sqrt{\dfrac{2M_iM_j}{M_j+M_i}}\left(\dfrac{\sigma_i+\sigma_j}{2}\right)^2\Omega_D} \tag{30}$$

$$\Omega_D = \frac{1.06036}{\left(\dfrac{k_bT}{\varepsilon_{i,j}}\right)^{0.1561}} + \frac{0.193}{\exp\left(0.47635\left(\dfrac{k_bT}{\varepsilon_{i,j}}\right)\right)} + \frac{1.03587}{\exp\left(1.52996\left(\dfrac{k_bT}{\varepsilon_{i,j}}\right)\right)} + \frac{1.76474}{3.89411\left(\dfrac{k_bT}{\varepsilon_{i,j}}\right)} \tag{31}$$

where ξ/ε is the ratio of tortuosity to porosity. r_p is the mean pore radius of the catalyst layer. D_{ij} is the binary diffusion coefficient of gas species i and j. σ is the mean characteristic length and Ω_D is a dimensionless diffusion collision term. k_b is the Boltzmann's constant (1.38066×10^{-23} J.K^{-1}). The values of σ_i and $\varepsilon_{i,j}$ can be obtained from reference (Reid *et al.* 1987) and are summarized in Table 1 (Reid *et al.* 1987).

The Darcy's law (Eqs. (32) and (33)) is used as source term in the momentum equations (Eqs. (19) and (20)).

$$S_x = -\frac{\mu U}{B_g} \tag{32}$$

$$S_y = -\frac{\mu V}{B_g} \tag{33}$$

B_g is the permeability (m^2) of the catalyst layer.   Typical value of permeability (i.e., $2 \times 10^{-10} m^2$) is used for the porous catalyst layer while infinitely large value (i.e., $10^{20} m^2$) is used for the fuel channel (Ni 2012b). By adjusting the permeability values, the momentum equations can be applied to both the fuel channel and the catalyst layer (Yuan *et al.* 2007a).

The source term (S_T :W m^{-3}) in energy equation (Eq. (21)) represents reaction heats from the chemical reactions (MCDR, MSR, and WGSR) and can be calculated by Eq. (34).

Table 1 Parameters for effective diffusion coefficient computation (Reid *et al.* 1987)

	CO	CO$_2$	H$_2$	O$_2$	CH$_4$	N$_2$	H$_2$O
σ_i	3.69	3.941	2.827	3.467	3.758	3.798	2.641
ε_i / k	91.7	195.2	59.7	106.7	148.6	71.4	809.1

$$S_T = R_{MCDR}H_{MCDR} + R_{MSR}H_{MSR} + R_{WGSR}H_{WGSR} \tag{34}$$

The source term in species equation (Eq. (22)) accounts for the mass consumption/generation by MCDR, MSR and WGSR reactions (Ni 2009). Considering that there are 5 gas species (CO$_2$, CH$_4$, CO, H$_2$, H$_2$O), the species equation should be applied to any 4 gas species (the molar fraction of the 5th gas species can be obtained due to $\sum X_i = 1$).   For CH$_4$, the source term (S_{CH_4}: kg m^{-3} s^{-1}) can be written as

$$S_{CH_4} = -R_{MCDR}M_{CH_4} - R_{MSR}M_{CH_4} \tag{35}$$

Similarly, the source terms for CO$_2$, CO, and H$_2$ can be written as

$$S_{CO_2} = -R_{MCDR}M_{CO_2} + R_{WGSR}M_{CO_2} \tag{36}$$

$$S_{CO} = 2R_{MCDR}M_{CO} + R_{MSR}M_{CO} - R_{WGSR}M_{CO} \tag{37}$$

$$S_{H_2} = 2R_{MCDR}M_{H_2} + 3R_{MSR}M_{H_2} + R_{WGSR}M_{H_2} \tag{38}$$

2.3 Numerical scheme

As a real reformer stack consists of many identical single compact reformers, periodical boundary condition is applied to the upper boundary (y=yM) (Ni 2012b, Yuan *et al*. 2007a). That is to say, there is no heat transfer between compact reformers through the upper boundary (zero heat flux). Since the focus is on the fuel reforming channel and catalyst layer, heat from the combustion channel is modeled as boundary condition (Yuan *et al*. 2007a). Therefore, a constant heat flux is specified at the lower boundary (y=0). At the inlet of the fuel channel, a constant velocity is specified while zero velocity is specified for the catalyst layer at the inlet and outlet (x = 0 and x = xL).

The governing equations in the CFD model can be solved with finite difference method (FDM), finite volume method (FVM), or finite element method (FEM) (Wang 2004). In the present study, the FVM is employed as it is a most widely used method for solving the fluid flow and heat transfer problems and is also widely used by commercial CFD software, such as FLUENT. The upwind scheme and central difference scheme are used to treat the convection terms and diffusion terms (Patankar 1980). The SIMPLEC algorithm is employed to link the velocity and pressure fields (Patankar 1980). The discretized equations are solved iteratively using the TDMA based scheme.

Computational starts from initialization. Initial gas velocity, temperature and gas composition are applied to the whole computational domain. Then the chemical sub-model is solved to determine the chemical reaction rates and corresponding reaction heats. Subsequently, the CFD model is solved with the source terms from the chemical sub-model. With updated flow field, temperature field, gas composition distribution, the chemical sub-model is solved again, followed by CFD model. Computation is repeated until convergence is achieved. The in-house code is written in FORTRAN. The CFD code has been validated rigorously by comparing the simulation results with data from the literature (Ni 2010).

3. Results and discussions

In this section, parametric simulations are performed to understand the coupled transport and reaction phenomena in a CR for hydrogen-rich gas production from CO2/CH4 mixture (molar ratio: 50/50). Operating and structural parameters are varied to investigate their effects on the CR performance. The simulation parameters are summarized in Table 2.

3.1 Base Case and comparison with experimental data from the literature

Fig. 3 shows the reaction rates of MCDR, MSR, WGSR, temperature and velocity in the CR for the base case: inlet temperature of 1073 K, inlet gas velocity of 1m.s-1, mean pore radius of 1 μm, and permeability of . It's found that the MCDR reaction rate is the highest near the inlet in the catalyst layer (Fig. 3(a)). Along the flow channel, the reaction rate decreases significantly. In addition, the reaction rate is found higher near the catalyst surface than deep inside the catalyst layer. This phenomenon is due to large temperature drop along the channel and lower CH4 molar fraction in the downstream and deep inside the catalyst layer, which will be discussed in the subsequent section. The peak MCDR reaction rate is found to be about 200molm-3s-1. The calculated MCDR reaction rate is consistent with the experimental data by Gokon *et al*. (2009). Moon and Ryu (2003) tested MCDR reaction on NiO-MgO catalyst at 1073 K. The measured reaction rate for CH4 is about 0.47. The thickness of the catalyst layer is about 20. Thus the

measured reaction rate is converted to be about 235mol.m-3.s-1, which is only slightly higher than the computed data. The agreement between the present numerical data and the experimental data from the literature validate the present model.

Table 2 Parameters used in base-case simulation

Parameter	Value
Operating temperature, T (K)	1073
Operating pressure, P (bar)	1.0
Porosity of the porous catalyst layer, ε	0.4
Tortuosity of the porous catalyst layer, ξ	3.0
Permeability of the porous catalyst layer, B_g, (m^2)	2×10^{-10}
Average pore radius, r_p (μm)	1.0
Thickness of the porous catalyst layer (cm)	0.4
Length of the Compact Reformer (cm)	10
Thickness of solid plate (cm)	0.1
Inlet velocity at the reforming duct: U_0 (m.s^{-1})	1.0
Height of the reforming duct (cm)	0.4

The reaction rate of WGSR is found to be negative in the catalyst layer (Fig. 3(b)), mainly due to a high concentration of CO2. Similar to MCDR, the highest WGSR reaction rate (-23.1mol.m-3.s-1) is found near the inlet.   The negative WGSR rate favors the H2O production in the catalyst layer, which in turn causes MSR reaction to occur (Fig. 3(c)). However, the reaction rate of MSR is negligibly small (0.73mol.m-3.s-1 the highest), due to low H2O production from the reversed WGSR. The temperature field in CR depends on the 3 chemical reactions (MCDR, MSR, and WGSR). In the present study, all 3 reactions consume heat because MCDR and MSR reactions are endothermic and the exothermic WGSR is reversed. As a result, the temperature in the CR decreases significantly along the main flow stream (Fig. 3(d)). Particularly in the catalyst layer, the temperature is decreased from 1073 K at the inlet to about 920 K at the outlet. This large temperature drop (particularly near the inlet) is mainly caused by MCDR reaction since its reaction rate is much higher than that of WGSR and MSR. The velocity contour (U/U0) is shown in Fig. 3(e). As can be seen, the velocity ratio (U/U0) increases from the wall to the core zone (axial center). The velocity in the catalyst layer is negligibly small as the permeability of the porous catalyst is small (2x10-10 m2).

The molar fractions of gas species in the CR are shown in Fig. 4. As expected, the molar fraction of CH4 and CO2 decreases considerably along the channel due to the MCDR reaction (Figs. 4(a) and (b)). For comparison, the molar fractions of CO and H2 increases long the main flow stream (Figs. 4(c) and (d)). Compared with CH4, CO2, and CO, the difference in molar fraction of H2 in the fuel channel and in the catalyst layer is much smaller, indicating fast diffusion of H2 through the catalyst layer. This phenomenon can be explained by high diffusion coefficient of H2 since its molecular weight is small (Eq. (29)).
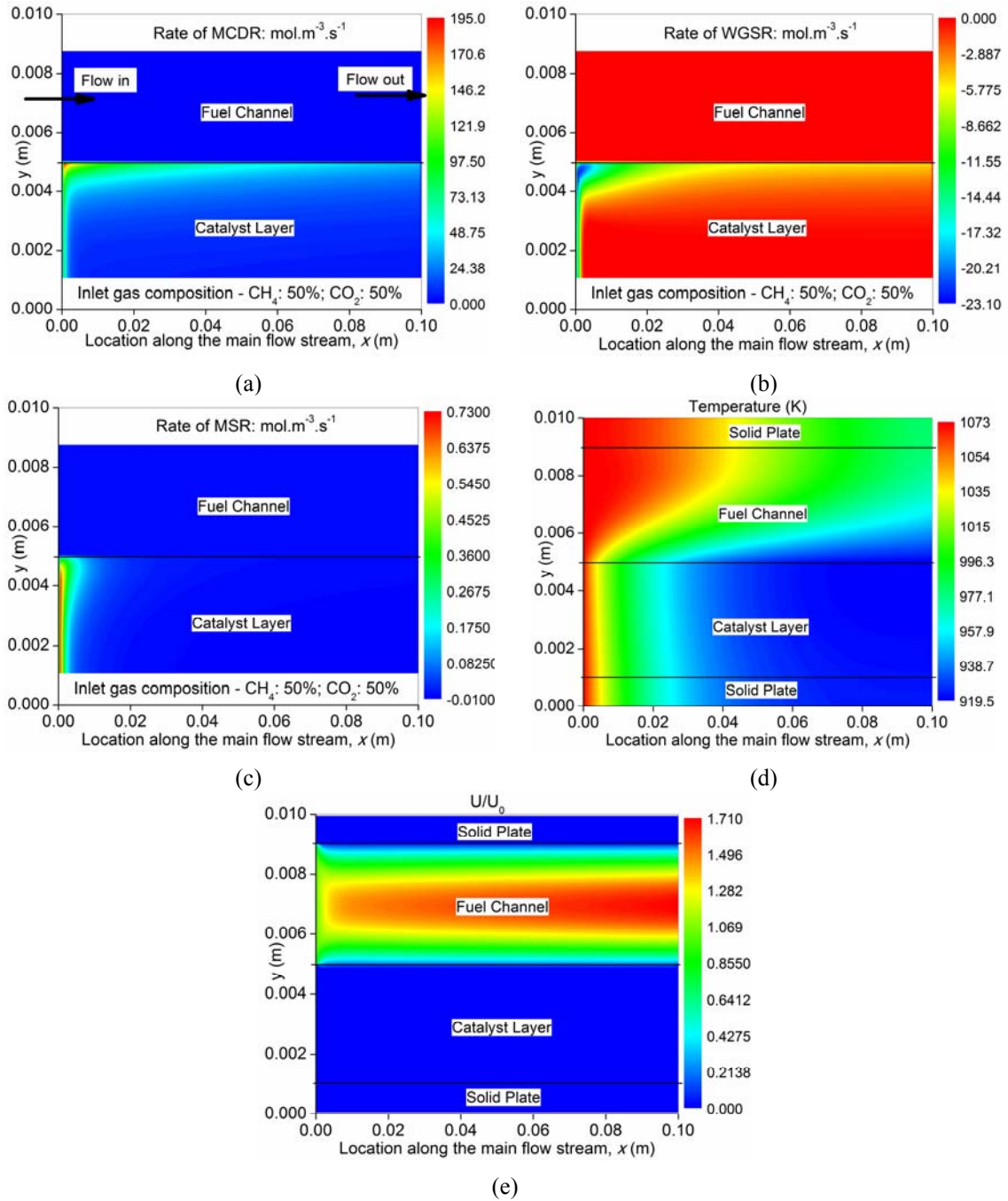
(a)

(b)

(c)

(d)

(e)

Fig. 3 Coupled transport and reaction in a CR at an inlet temperature of 1073 K, inlet gas velocity of 1m.s^{-1}; and heat supply rate of 10 kW.m^{-2} (base case) – (a) reaction rate of MCDR, (b) reaction rate of WGSR, (c) reaction rate of MSR, (d) temperature and (e) velocity ratio – U/U$_0$
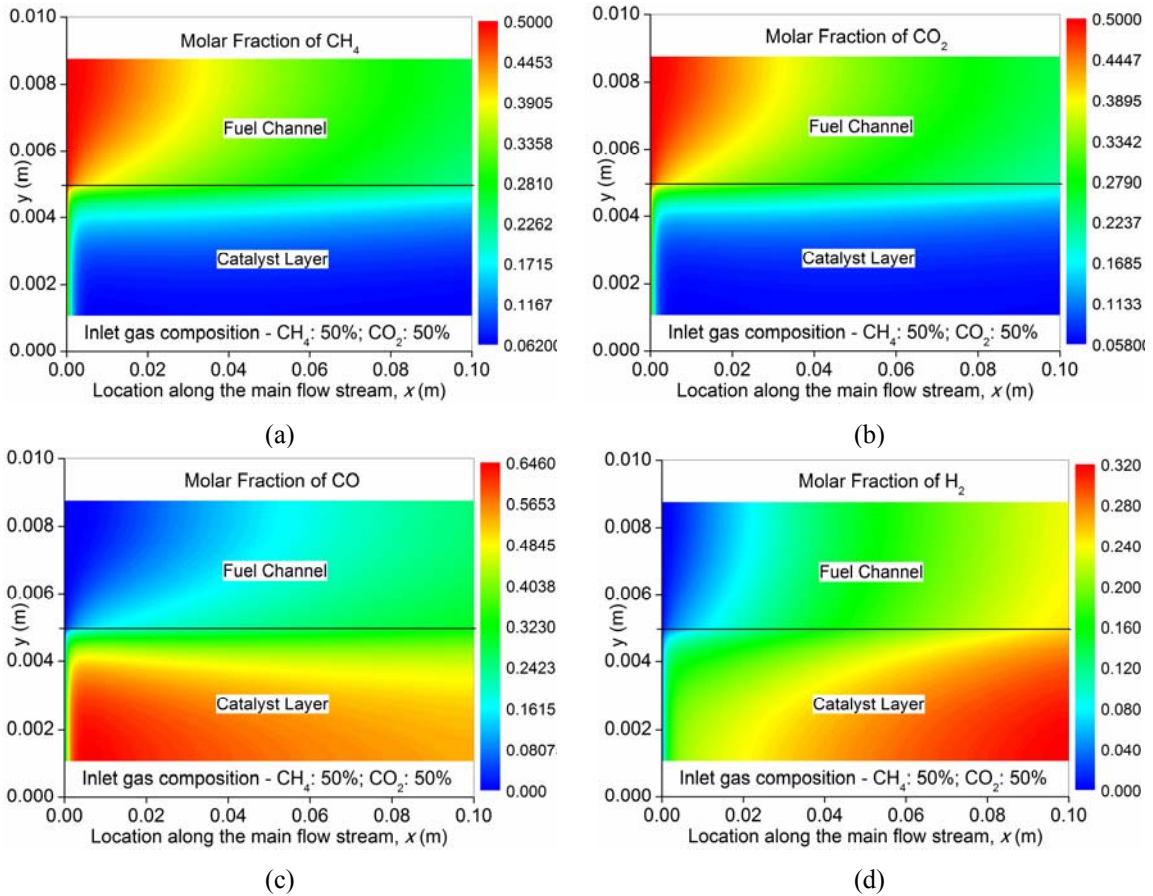
Fig. 4 Gas molar fractions in the CR for the base case – (a) CH_4, (b) CO_2, (c) CO and (d) H_2

3.2. Effect of inlet temperature

Simulations are performed at an inlet temperature of 973 K and 1173 K to examine the temperature effect on CR performance. The distributions of reaction rates and temperature in CRs are shown in Fig. 5. The reaction rates of MCDR and WGSR are found to be considerably higher at 1173 K than at 973 K (Figs. 5(a)-(d)). For example, the highest reaction rates of MCDR at an inlet temperature of 973 K and 1173 K are 135 mol.m-3.s-1 and 255 mol.m-3.s-1, respectively (Figs. 5(a) and b). The WGSR reaction rate is more sensitive to the temperature, as the highest reaction rates are -5.88 mol.m-3.s-1 at 973 K and -69.4 mol.m-3.s-1 at 1173 K (Figs 5(c) and (d)).

The temperature effect is easy to understand from the formulas for MCDR (Eqs. (4)-(7)) and WGSR reaction (Eqs. (11)-(14)). The present simulations also predict that higher temperature favors reversed WGSR, which is consistent with experimental observations.

For both 973 K and 1173 K cases, large temperature drops are observed near the inlet (Figs. 5(e) and (f)), due to high MCDR reaction rates. Since the reaction rates are higher at a higher temperature, larger temperature reduction along the CR is found for 1173 K than for 973 K cases.
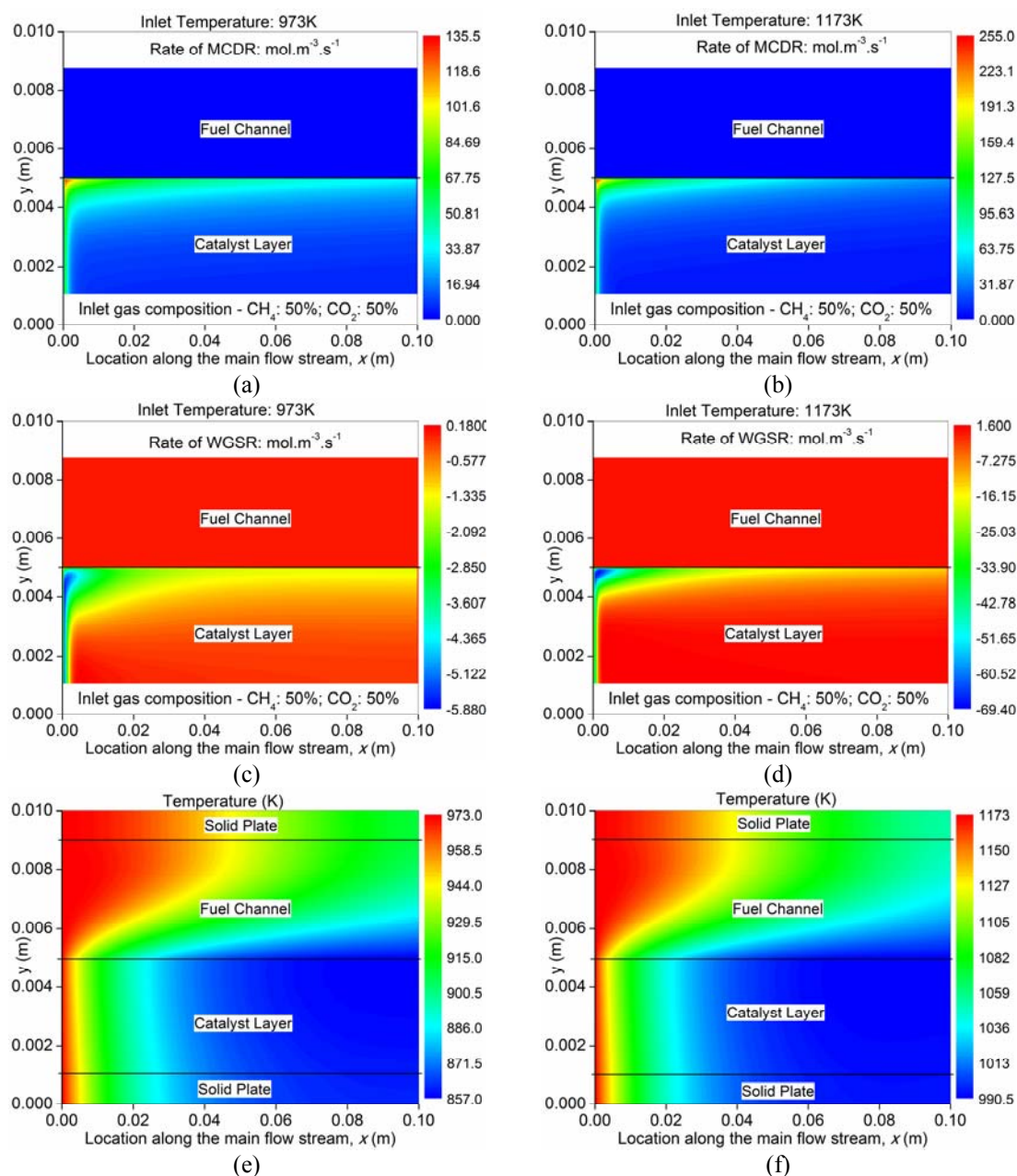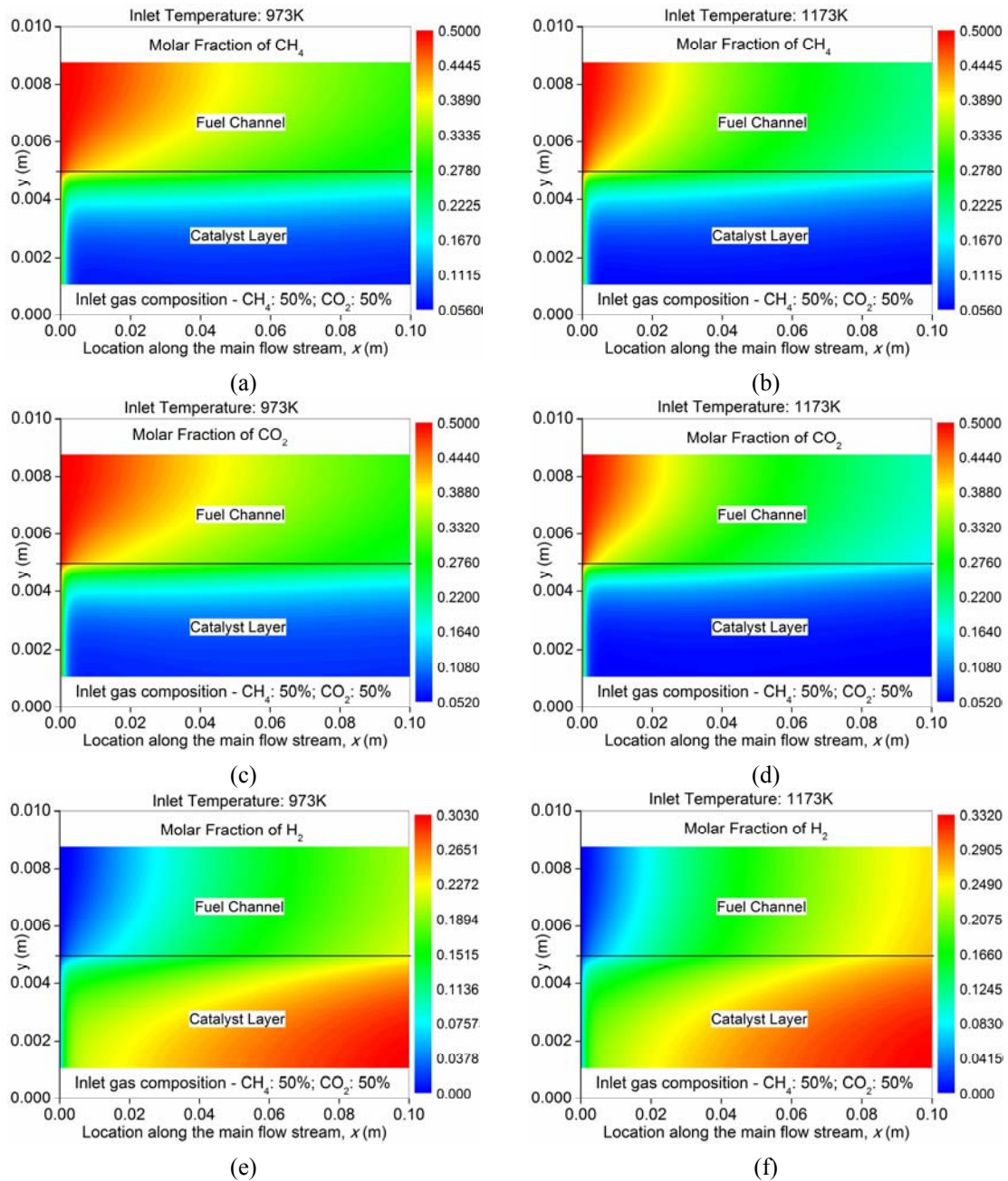
Fig. 5 Effect of inlet temperature on the transport and reaction in a CR – (a) reaction rate of MCDR at 973 K, (b) reaction rate of MCDR at 1173 K, (c) reaction rate of WGSR at 973, (d) reaction rate of WGSR at 1173 K, (e) temperature at 973 K and (f) temperature at 1173 K

For example, the temperature difference between the inlet and out of the catalyst layer is about 116 K for the 973 K case (from 973 K at the inlet to 857 K at the outlet) (Fig. 5(e)). For comparison, the temperature drop for the 1173 K case is about 183 K (Fig. 5(f)). The results

indicate that high heat flux should be supplied to the fuel reforming side if high operating temperature is used.

(a)

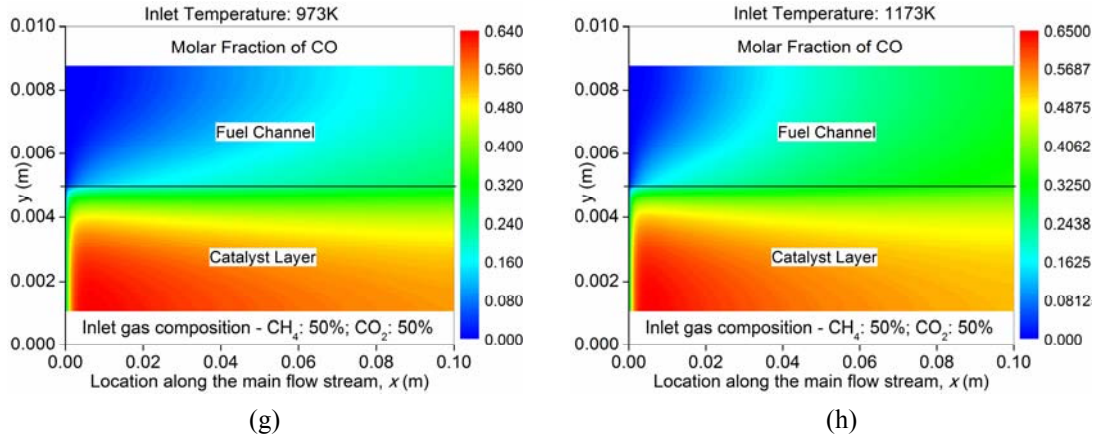(b)

(c)

(d)

(e)

(f)

Continued

(g)   (h)

Fig. 6 Molar fractions of gas species in a CR at different inlet temperatures – (a) CH_4 at 973 K, (b) CH_4 at 1173 K, (c) CO_2 at 973 K, (d) CO_2 at 1173 K, (e) H_2 973 K, (f) H_2 at 1173 K, (g) CO at 973 K and (h) CO at 1173 K

As the rates of MCDR and reversed WGSR reactions are much higher at 1173 K than at 973 K, more CH4 and CO2 are consumed and more CO and H2 are produced at 1173 K. As a result, larger gas composition variations are observed along the fuel reforming channel at 1173 K than at 973 K (Figs. 6(a)-(h)). For example, the molar fraction of H2 is increased from 0 at the inlet to about 26% at the outlet of the fuel channel at 1173 K (Fig. 6(f)). For comparison, the H2 molar fraction at the outlet of fuel reforming channel is about 20% at 973 K (Fig. 6(e)). In a word, increasing the inlet temperature greatly increases the reaction rates (MCDR and reversed WGSR), temperature gradient, and variation in gas molar fractions along the fuel reforming channel.

3.3. Effect of catalyst layer thickness

The thickness of the catalyst layer is changed from 4 mm to 2 mm and 6 mm to examine its effect on CR performance. As can be seen from Fig. 7(b), the MCDR reaction rates decrease considerably along the CR fuel channel with a thicker catalyst layer (6 mm). For comparison, the MCDR reaction rates decrease less significantly in the downstream of CR with a thinner catalyst layer (2 mm) (Fig. 7(a)). Due to a small thickness (2 mm), the MCDR reaction is non-negligible in the whole catalyst layer, even in downstream, the MCDR reaction rate is still about 40 mol.m-3.s-1 (Fig. 7(a)). For comparison, the MCDR reaction rate in the downstream is below 20 mol.m-3.s-1 even near the catalyst surface for the 6mm case (Fig. 7(b)). In addition, the MCDR reaction rate in the deep thick catalyst layer (6 mm) is in general below 10 mol.m-3.s-1, indicating that the thick catalyst layer is not fully utilized. The reversed WGSR reaction rates show less reduction along the fuel channel with a thicker catalyst layer (Fig. 7(d)) than with a thinner layer (Fig. 7(c)). With a thin catalyst layer (2 mm), the temperature in the catalyst layer is decreased from 1073 K at the inlet to 911 K at the outlet (Fig. 7(e)). For comparison, the temperature drop in the catalyst layer with a larger thickness (6 mm) is considerably smaller (about 956 K at the outlet) due to lower MCDR reaction rate in the downstream (Fig. 7(f)).
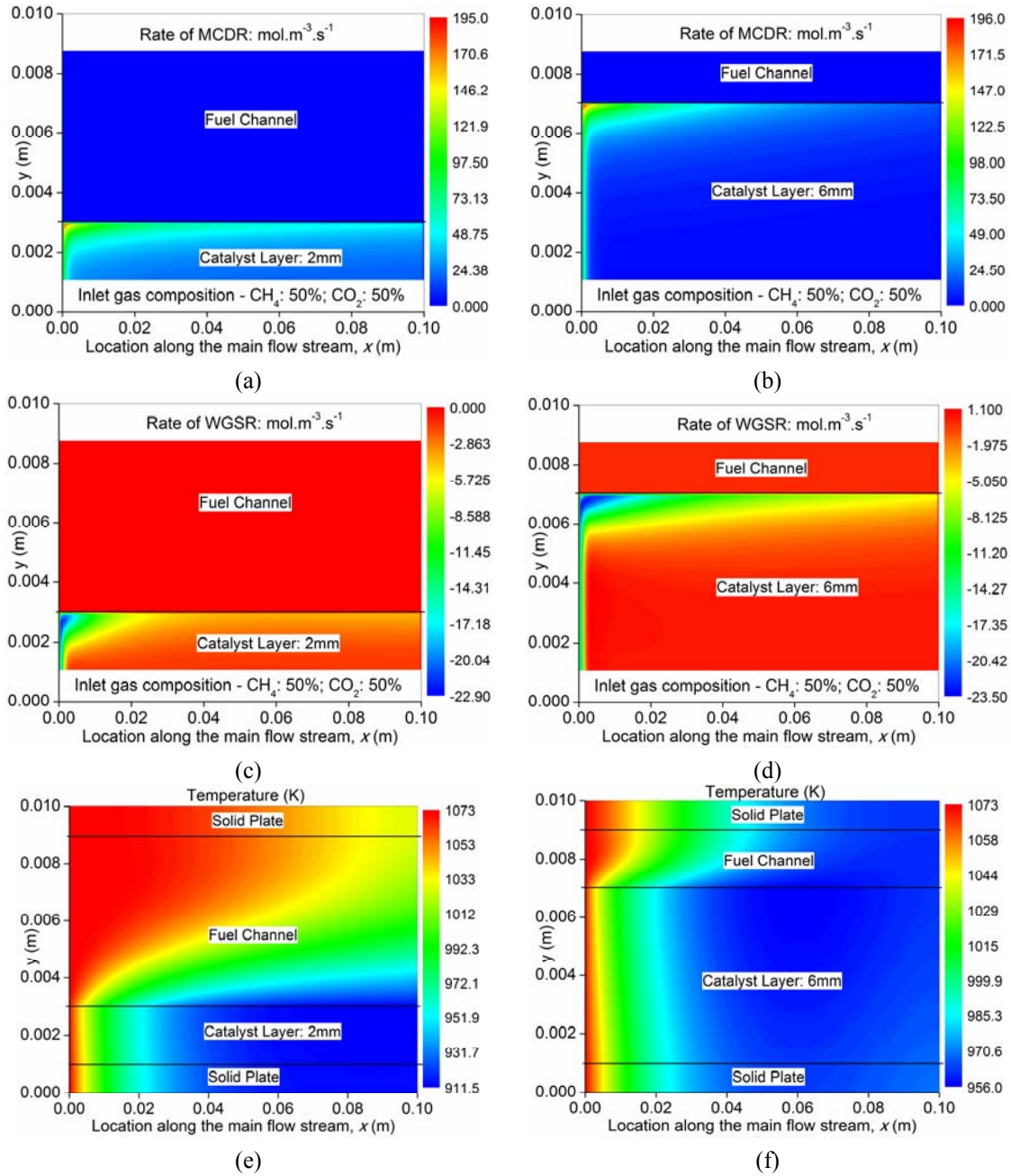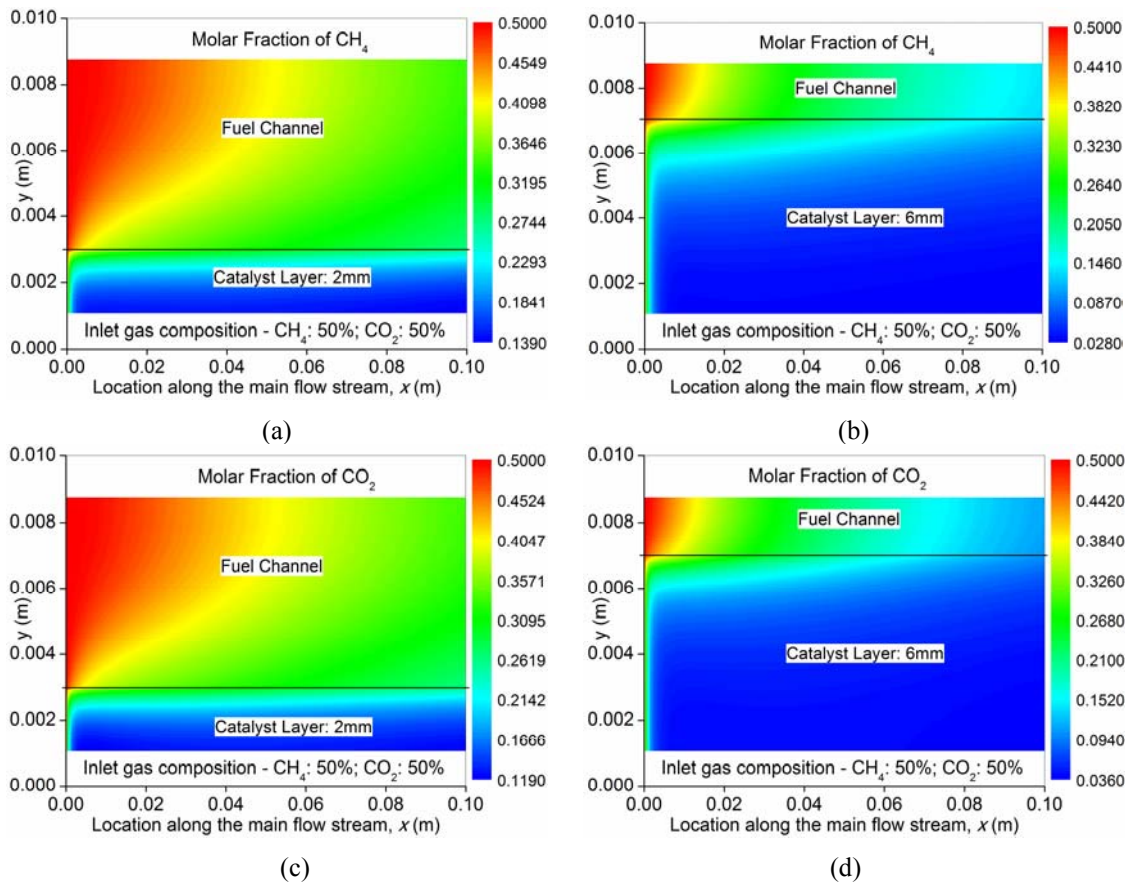
Fig. 7 Effect of catalyst layer thickness (2 mm and 6 mm) on the transport and reaction in a CR – (a) reaction rate of MCDR, catalyst layer 2 mm, (b) reaction rate of MCDR, catalyst layer 6 mm, (c) reaction rate of WGSR, catalyst layer 2 mm, (d) reaction rate of WGSR, catalyst layer 6 mm, (e) temperature, catalyst layer 2 mm and (f) temperature, catalyst layer 6 mm

Despite of larger MCDR reaction rate, the variation of CH4 molar fraction in the fuel reforming channel is smaller for a thin catalyst layer than a thick catalyst layer (Figs. 8(a) and (b)). This is because the rate of gas supply (larger cross-sectional area) is higher for a thinner catalyst layer. Similarly, the molar fractions of CO2, H2 and CO all show larger variations along the fuel reforming channel with a thicker (6 mm) catalyst layer (Figs. 8(c)-(f)).

From the present simulation, it can be seen that thick catalyst layer can achieve high fuel conversion, but the catalyst layer is not fully utilized. If expensive noble metal catalyst is used, there will be an optimal catalyst layer thickness considering economics and conversion efficiency.

(a)

(b)

(c)

(d)

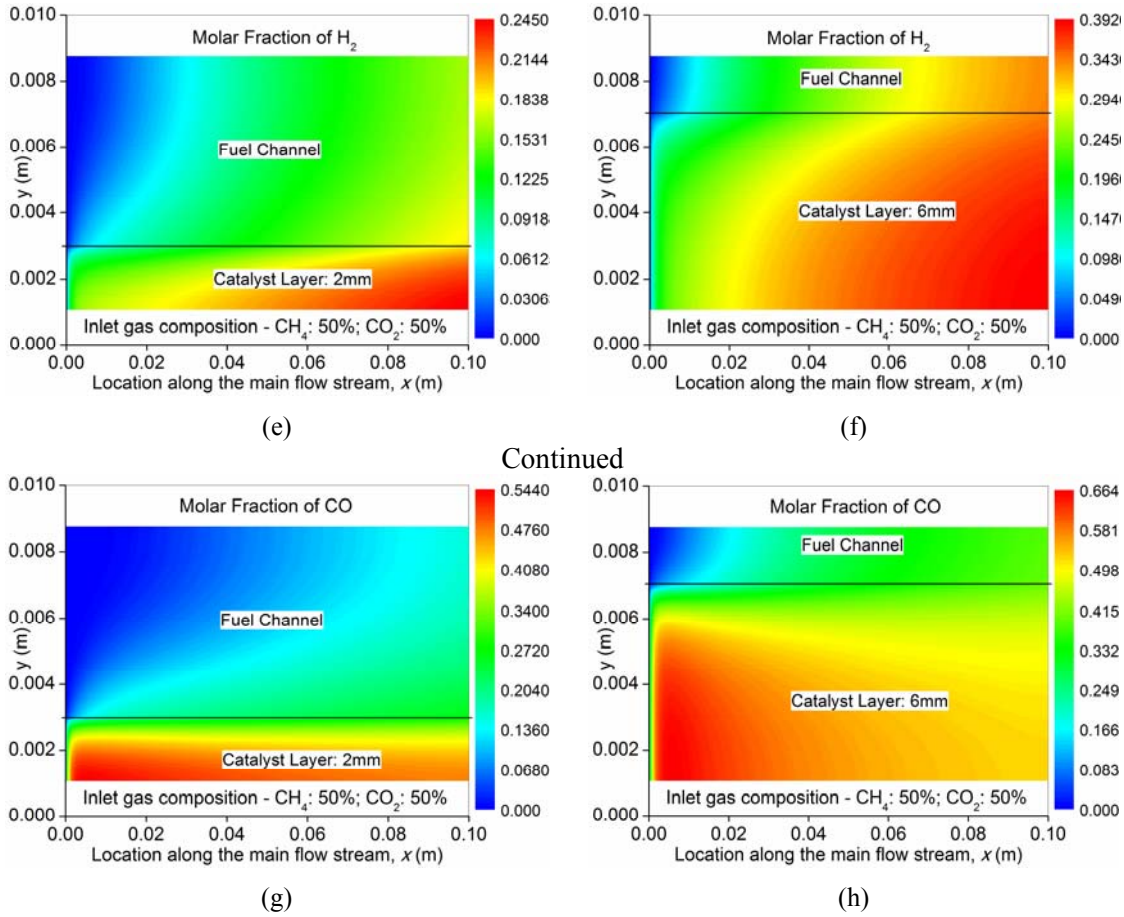Continued

(e)

Continued

(f)

(g)

(h)

Fig. 8 Molar fractions of gas species in a CR with different catalyst layer thicknesses (2 mm and 6 mm) – (a) CH_4, catalyst layer 2 mm, (b) CH_4, catalyst layer 6 mm, (c) CO_2, catalyst layer 2 mm, (d) CO_2, catalyst layer 6 mm, (e) H_2, catalyst layer 2 mm, (f) H_2, catalyst layer 6 mm, (g) CO, catalyst layer 2 mm and (h) CO, catalyst layer 6 mm

3.4. Effect of inlet gas composition

In this section, the performance of a CR with an inlet gas composition of 50% CH_4, 25% CO_2, and 25% H_2O is simulated. The reaction rates and temperature in the CR are shown in Fig. 9 while the molar fractions of gas species are shown in Fig. 10. The MCDR reaction rate is considerably lower (Fig. 9(a)) than the base case (Fig. 3) while the MSR reaction rate (Fig. 9(b)) is higher than the base case (Fig. 3). However, the computed peak MSR reaction rate (12.8 mol.m^{-3}.s^{-1}) is still much lower than the MCDR reaction rate (110 mol.m^{-3}.s^{-1}). This is because part of the H_2O is consumed by WGSR, as can be seen from the positive WGSR (Fig. 9(c)). Since the MCDR reaction rate is considerably lower than the base case and the WGSR reaction rate is positive, the temperature drop in the catalyst layer is smaller than the base case (Fig. 9(d)). For example, the

temperature at the outlet of the catalyst layer is about 948 K, higher than 919 K in the base case (Fig. 3(d)). The molar fractions of gas species are shown in Fig. 10. As can be seen from Fig. 10(c), the H_2 molar fraction (Fig. 10(c)) in the fuel reforming channel is higher than that in the base case (Fig. 4(d)). The high H_2 molar fraction in the present case is because: (1) MSR tends to generate more H_2 than MCDR (Eqs. (1) and (3)); (2) positive WGSR produces H_2. As a result, the H_2 molar fraction at the outlet of the fuel reforming channel is over 0.3, considerably higher than the base case (about 0.24). Since WGSR is positive in the present case, the molar fraction of CO is found to be lower than the base case (Figs. 10(d) and 4(c)). For example, CO molar fraction at the outlet of the fuel reforming channel is about 0.2, while it's about 0.28 in the base case (Fig. 4(c)). The results reveal that the fuel conversion selectivity can be controlled by adjusting the inlet gas composition. High H_2 yield and low CO generation can be achieved by supplying more H_2O and less CO_2 to the CR.
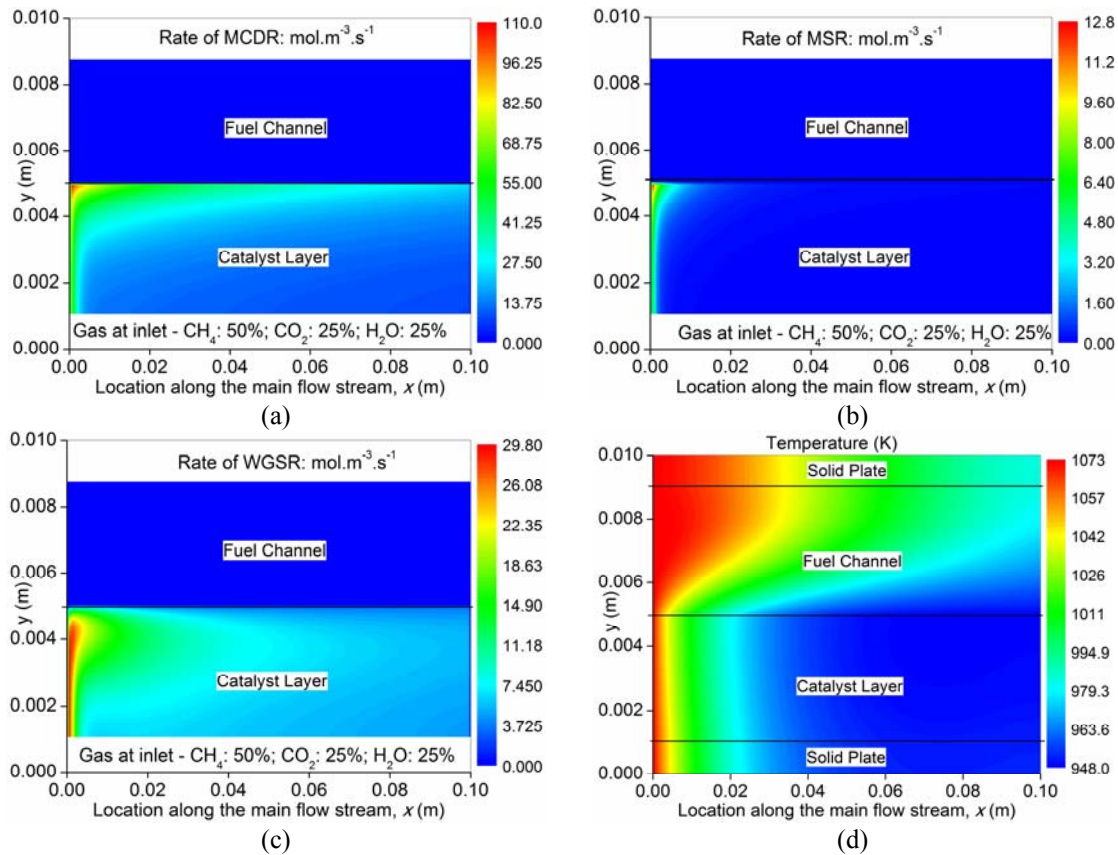

Fig. 9 Inlet gas composition: 50% CH_4; 25% CO_2 and 25% H_2O – (a) reaction rate of MCDR, (b) reaction rate of MSR, (c) reaction rate of WGSR and (d) temperature

3.5. Effect of catalyst layer permeability

The permeability of the porous catalyst layer is changed from 2×10^{-10} m^2 to 2×10^{-7} m^2 and 2×10^{-13} m^2 to examine its influence on the transport and reaction in a CR. As can be seen from Fig. 11a for CR with lower permeability (2×10^{-13} m^2), the velocity in the fuel reforming channel increases from the wall or surface of catalyst layer to the axial line of the channel, very similar to conventional fully developed channel flow. The velocity in the porous catalyst layer is almost zero, indicating that the gas transport in the catalyst layer is dominated by diffusion. The computed velocity distribution is consistent with the flow field in a reforming duct [22]. For comparison, a larger permeability (2×10^{-7} m^2) facilitates gas permeation into the catalyst layer (Fig. 11(b)).

Thus the transport of gas species is governed by both convection and diffusion. Due to the enhanced gas transport in the catalyst layer with a larger permeability (2×10^{-7} m^2), the MCDR reaction rate is also slightly enhanced (Figs. 11(c) and (d)), leading to slightly larger temperature drop in the catalyst layer (Figs. 11(e) and (f)).
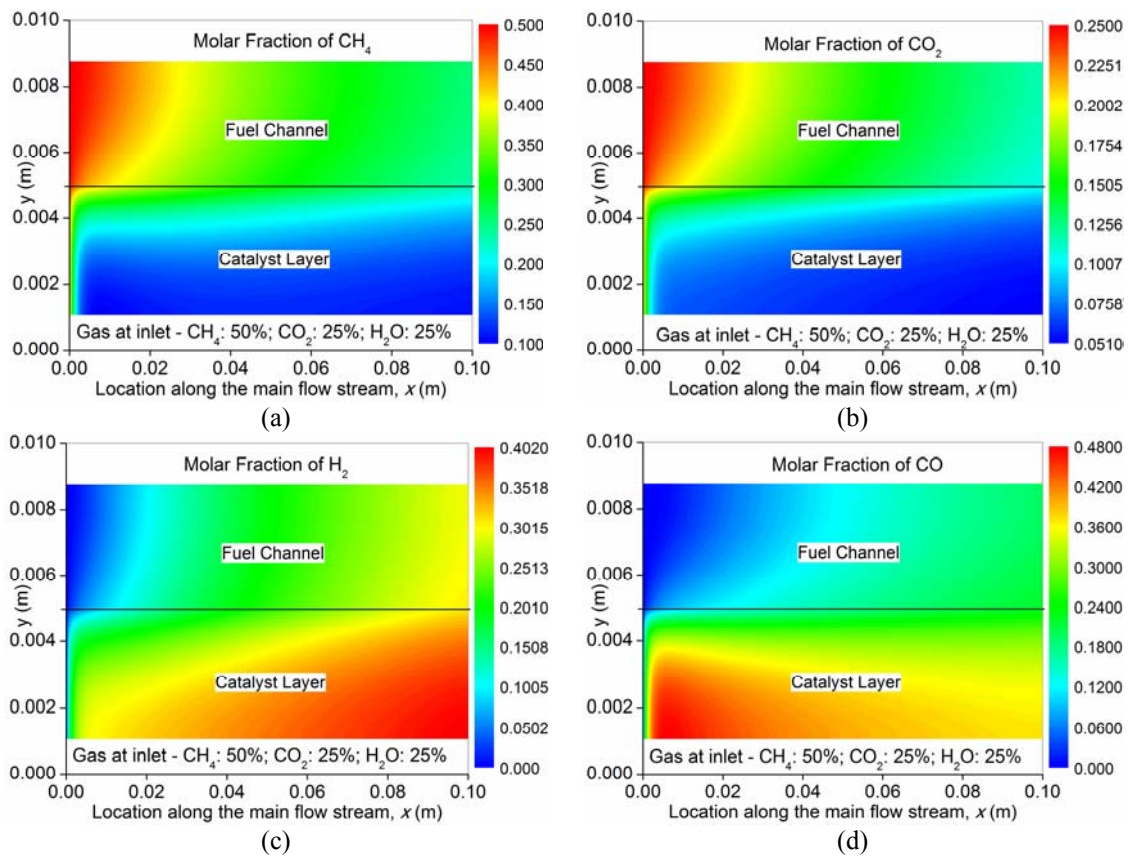

Fig. 10 Molar fractions of gas species in a CR with inlet gas composition: 50% CH_4; 25% CO_2 and 25% H_2O – (a) CH_4; (b) CO_2; (c) H_2; and (d) CO
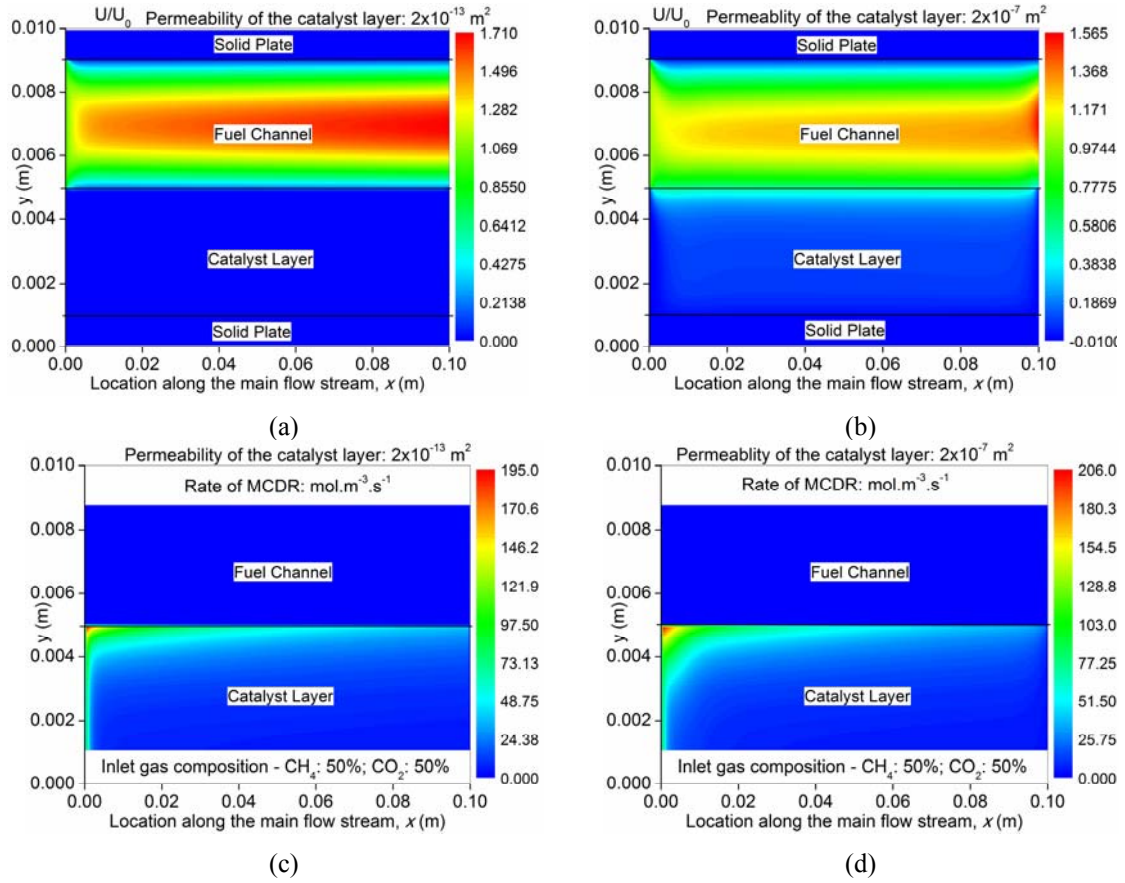
Fig. 11 Effect of catalyst layer permeability ($2\times10^{-13}m^2$ and $2\times10^{-7}m^2$) on the transport and reaction in a CR – (a) velocity ratio – U/U_0 at $2\times10^{-13}m^2$, (b) velocity ratio – U/U_0 at $2\times10^{-7}m^2$, (c) reaction rate of MCDR at $2\times10^{-13}m^2$, (d) reaction rate of MCDR at $2\times10^{-7}m^2$, (e) temperature at $2\times10^{-13}m^2$ and (f) temperature at $2\times10^{-7}m^2$.

4. Conclusions

This paper reports a numerical study on a CR used for methane carbon dioxide reforming for syngas production with a 2D heat and mass transfer model. The model considers the MCDR, MSR and WGSR in the porous catalyst layer and the heat/mass transfer in CR. The model is solved with an in-house code based on the FVM, which has been validated extensively by comparing the numerical data with data from the literature.

Parametric simulations are performed to investigate the coupled transport and reaction phenomena and the effects of various operating/structural parameters on the CR performance. Fed with 50% CH_4 and 50% CO_2, the MCDR is the dominating reaction in the CR. The computed reaction rate is consistent with experimental data from the literature, validating the present model.

The reaction rates of MCDR and reversed WGSR are found to decrease considerably along the channel due to large temperature drop and fuel conversion. Increasing the inlet temperature considerably increases the reaction rates, temperature gradient and variation in gas composition along the channel. It's found that increasing the catalyst layer thickness is beneficial to increase the fuel conversion but the catalyst layer may not be fully utilized if it's too thick. Thus there must be an optimal catalyst thickness considering both the conversion and economics. It's also found that a high H_2 yield can be achieved by supplying more H_2O and less CO_2 at the inlet. In addition, increasing the permeability of the catalyst layer enhances convection in the porous layer, leading to slightly enhanced reaction rates.

Based on the present model and results, future works can be conducted to optimize the CR catalyst layer to achieve desired syngas production. The 2D model can be extended to a 3D model and include the combustion channel for more detailed study and system optimization.

Acknowledgements

References

Abashar, M.E.E., Alhumaizi, K.I. and Adris, A.M. (2003), "Investigation of methane-steam reforming in fluidized bed membrane reactors", *Chem. Eng. Res. Des.,* **81**(2), 251-258.

Ahmed, K. and Foger, K. (2010), "Fuel processing for high temperature high efficiency fuel cells", *Ind. Eng. Chem. Res.*, **49**(16), 7239-7256.

Al-Baghdadi, M.A.R.S. and Al-Janabi, H.A.K.S. (2007), "Influence of the design parameters in a proton exchange membrane (PEM) fuel cell on the mechanical behavior of the polymer membrane", *Energy Fuels*, **21**(4), 2258-2267.

Chase, M.W. (1998), *NIST-JANAF thermochemical tables*, (4th Ed.), American Chemical Society, American Institute of Physics for the National Institute of Standards and Technology.

Chanburanasiri, N., Ribeiro, A.M. and Rodrigues, A.E., Laosiripojana, N. and Assabumrungrat, S. (2013), "Simulation of methane steam reforming enhanced by in situ CO2 sorption utilization K2CO3 promoted hydrotalcites for H2 production", *Energy Fuels,* in press. **DOI:** 10.1021/ef302043e.

Gallucci, F., Fernandez, E., Corengia, P.van S. and Annaland, M. (2013), "Recent advances on membranes and membrane reactors for hydrogen production", *Chem. Eng. Sci.*, in press.

Gokon, N., Osawa, Y., Nakazawa, D. and Kodama, T. (2009, "Kinetics of CO_2 reforming of methane by catalytically activated metallic foam absorber for solar receiver-reactors", *Int. J. Hydrogen Energ.*, **34,** 1787-1800.

Goula, G., Kiousis, V., Nalbandian, L. and Yentekakis, I.V. (2006), "Catalytic and electrocatalytic behavior of Ni-based cermet anodes under internal dry reforming of CH4+CO2 mixtures in SOFCs", *Solid State Ionics,* **177**, 2119-2123.

Haberman, B.A. and Young, J.B. (2004), "Three-dimensional simulation of chemically reacting gas flows in the porous support structure of an integrated-planar solid oxide fuel cell", *Int. J. Heat Mass Transfer,* **47**, 3617-3629.

Halabi, M.H., Croon, M.H.J.M.D., Shaaf, J Van Der, Cobden, P.D. and Schouten, J.C. (2008), "Modeling and analysis of autothermal reforming of methane to hydrogen in a fixed bed reformer", *Chem. Eng. J.,* **137**(3), 568-578.

Hosseini, S., Danilov, V.A., Vijay, P. and Tade, M.O. (2011), "Improved tank in series model for the planar solid oxide fuel cell", *Ind. Eng. Chem. Res.*, **50**(2), 1056-1069.

Huang, T., Huang, W., Huang, J. and Ji, P. (2011), "Methane reforming reaction with carbon dioxide over SBA-15 supported Ni-Mo bimetallic catalysts", *Fuel Process. Technol.*, **92**(10), 1868-1875.

Lebouvier, A., Cauneau, F. and Fulcheri, L. (2011), "2D axisymmetric coupled computational fluid dynamics-kinetics modeling of a nonthermal arc plasma torch for diesel fuel reforming", *Energy Fuels*, **25**(7), 2833-2840.

Lemonidou, A.A., Goula, M.A. and Vasalos, I.A. (1998), "Carbon dioxide reforming of methane over 5 wt.% nickel calcium aluminate catalysts – effect of preparation method", *Catalysis Today*, **46**(2-3), 175-183.

Li, X.S., Zhu, B., Shi, C., Xu, Y. and Zhu, A.M. (2011), "Carbon dioxide reforming of methane in kilohertz spark-discharge plasma at atmospheric pressure", *AICHE J.*, **57**(10), 2854-2860.

Lim, L.T., Chadwick, D. and Kershenbaum, L. (2005), "Achieving autothermal operation in internally reformed solid oxide fuel cells: simulation studies", *Ind. Eng. Chem. Res.*, **44**(25), 9609-9618.

Lulianelli, A., Manzolini, G., Falco, M.D., Campanari, S., Longo, T., Liguori, S. and Basile, A. (2010), "H2 production by low pressure methane reforming in a Pb-Ag membrane reactor over a Ni-based catalyst: experimental and modeling", *Int. J. Hydrogen Energy*, **35**(20), 11514-11524.

Mermelstein, J., Brandon, N. and Millan, M. (2009), "Impact of steam on the interaction between biomass gasification tars and nickel-based solid oxide fuel cell anode materials", *Energy Fuels,* **23**(10), 5042-5058.

Moon, D.J. and Ryu, J.W. (2003), "Electrocatalytic reforming of carbon dioxide by methane in SOFC system", *Catalysis Today*, **87**, 255-264.

Ni, M., Leung, M.K.H., Sumathy, K. and Leung, D.Y.C. (2006), "Potential of renewable hydrogen production for energy supply in Hong Kong", *Int. J. Hydrogen Energy*, **31**(10), 1401-1412.

Ni, M., Leung, M.K.H., Leung, D.Y.C. and Sumathy, K. (2007), "A review and recent developments in photocatalytic water-splitting using TiO2 for hydrogen production", *Renew. Sust. Energ. Rev.*, **11**, 401-425.

Ni, M., Leung, M.K.H. and Leung D.Y.C. (2008), "Technological development of hydrogen production by solid oxide electrolyzer cell (SOEC)", *Int. J. Hydrogen Energy*, **33**(9), 2337-2354.

Ni, M. (2009), "On the source terms of species equations in fuel cell modeling", *Int. J. Hydrogen Energy*, **34**, 9543-9544.

Ni, M. (2010), "2D thermal-fluid modeling and parametric analysis of a planar solid oxide fuel cell", *Energy Conversion Manage.,* **51**, 714-721.

Ni, M. (2011), "Thermo-electrochemical modelling of ammonia-fueled solid oxide fuel cells considering ammonia thermal decomposition in the anode", *Int. J. Hydrogen Energy*, **36**, 2027-2036.

Ni, M. (2012a), "2D thermal modeling of a solid oxide electrolyzer cell (SOEC) for syngas production by H_2O/CO_2 co-electrolysis", *Int. J. Hydrogen Energy*, **37**, 6389-6399.

Ni, M. (2012b), "Modeling of SOFC running on partially pre-reformed gas mixture", *Int. J. Hydrogen Energy*, **37**, 1731-1745.

Papadam, T., Goula, G. and Yentekakis I.V. (2012), "Long-term operation stability tests of intermediate and high temperature Ni-based anodes' SOFCs directly fueled with simulated biogas mixtures", *Int. J. Hydrogen Energy*, **37**, 16680-16685.

Patankar, S.V. (1980), *Numerical heat transfer and fluid flow*, McGraw-Hill, New York.

Qi, Y.T., Huang, B. and Luo, J.L. (2008), "1-D dynamic modeling of SOFC with analytical solution for reacting gas-flow problem", *AICHE J.*, **54**(6), 1537-1553.

Rady, A.C., Giddey, S., Badwal, S.P.S., Ladewig, B.P. and Bhattacharya, S. (2012), "Review of fuels for direct carbon fuel cells", *Energy Fuels*, **26**(3), 1471-1488.

Reid, R.C., Prausnitz, J.M., Poling, B.E. (1987), *The properties of gases & liquids* (4th Ed.), McGraw-Hill Book Company, New York.

Richardson, J.T. and Paripatyadar, S.A. (1990), Carbon dioxide reforming of methane with supported rhodium. *Appl.Catalysis*, **61**(1), 293-309.

Scheffe, J.R. and Steinfeld, A. (2012), "Thermodynamic analysis of cerium-based oxides for solar thermochemical fuel production", *Energy Fuels*, **26**(3), 1928-1936.

Soloviev, S.O., Kapran, A.Y., Orlyk, S.N. and Gubareni, E.V. (2011), "Carbon dioxide reforming of methane on monolithic Ni/Al$_2$O$_3$-based catalysts", *J. Natural Gas Chemistry*, **20**, 184-190.

Wang, C.Y. (2004), "Fundamental models for fuel cell engineerin", *Chem. Rev.,* **104**, 4727-4765.

Wang, H.Z., Leung, D.Y.C., Leung, M.K.H. and Ni, M. (2010), "Modeling of parasitic hydrogen evolution effects in an aluminum-air cell", *Energy Fuels*, **24**(7), 3748-3753.

Yu, X.P., Wang, N., Chu, W. and Liu, M. (2012), "Carbon dioxide reforming of methane for syngas production over La-promoted NiMgAl catalysts derived from hydrotalcites", *Chem. Eng. J.*, **209**, 623-632.

Yuan, J.L., Rokni, M. and Sunden, B. (2003), "Three-dimensional computational analysis of gas and heat transport phenomena in ducts relevant for anode-supported solid oxide fuel cells", *Int. J. Heat Mass Transfer*, **46**, 809-821.

Yuan, J.L., Lv, X.R., Sunden, B. and Yue, D.T. (2007a), "Analysis of parameter effects on transport phenomena in conjunction with chemical reactions in ducts relevant for methane reformer", *Int. J. Hydrogen Energy*, **32**(16), 3887-3898.

Yuan, J.L., Ren, F. and Sunden, B. (2007b), "Analysis of chemical-reaction-coupled mass and heat transport phenomena in a methane reformer duct for PEMFCs", *Int. J. Heat Mass Transfer*, **50**, 687-701.

Yuan, J.L., Yang, G.G. and Sunden, B. (2010), "On reaction coupled transport phenomenon in reformer ducts", *Int. J. Hydrogen Energy*, **35**(13), 7183-7188.

Zanfir, M. and Gavriilidis, A. (2003), "Catalytic combustion assisted methane steam reforming in a catalytic plate reactor", *Chem.Eng. Sci.*, **58**, 3947-3960.

Zeppieri, M., Villa, P.L., Verdone, N., Scarsella, M. and Filippis, P.D. (2010), "Kinetic of methane steam reforming reaction over nickel- and rhodium-based catalysts", *Applied Catalysis A: General,* **387**(1-2), 147-154.

Nomenclature

B_g	Permeability of catalyst layer, m^2
c_p	Heat capacity, $kJ\ kg^{-1}\ K^{-1}$
D_i^{eff}	Effective diffusion coefficient of species i, $m^2\ s^{-1}$
$D_{i,k}$	Knudsen diffusion coefficient of i, $m^2\ s^{-1}$
$D_{i,j}$	Binary diffusion coefficient of i and j, $m^2\ s^{-1}$
F	Faraday constant, $C\ mol^{-1}$
k	Thermal conductivity, $W\ m^{-1}\ K^{-1}$
M_i	Molecular weight of species i, $kg\ mol^{-1}$
P	Operating pressure, atm
R	Universal gas constant, $kJ\ mol^{-1}\ K^{-1}$
R_{MCDR}	Rate of methane carbon dioxide reforming (MCDR) reaction, $mol\ m^{-3}\ s^{-1}$
R_{MSR}	Rate of methane steam reforming (MSR) reaction, $mol\ m^{-3}\ s^{-1}$
R_{WGSR}	Rate of water gas shift reaction (WGSR), $mol\ m^{-3}\ s^{-1}$
r_p	Mean pore radius of the catalyst layer, m
S_m	Source term in continuity equation, $kg\ m^{-3}\ s^{-1}$
$S_x,\ S_y$	Source terms in momentum equations, $kg\ m^{-2}\ s^{-2}$
S_T	Source term in energy equation, $W\ m^{-3}$
S_{sp}	Source term in species equations, $kg\ m^{-3}\ s^{-1}$
T	Operating temperature, K
U	Velocity in x direction, $m\ s^{-1}$
U_0	Gas velocity at the inlet, $m\ s^{-1}$
V	Velocity in y direction, $m\ s^{-1}$
X_i	Molar fraction of species i
Y_i	Mass fraction of species i
μ	Viscosity, $kg\ m^{-1}\ s^{-1}$
ε	Porosity of the catalyst layer
ξ	Tortuosity of the catalyst layer
Ω_D	Dimensionless diffusion collision integral
ρ	Density of the gas mixture, $kg\ m^{-3}$